Nanoscale

Analyzing fidelity and reproducibility of DNA templated plasmonic nanostructures

Journal:	*Nanoscale*
Manuscript ID	NR-ART-04-2019-003711.R1
Article Type:	Paper
Date Submitted by the Author:	12-Aug-2019

Complete List of Authors:	Mathur, Divita; US Naval Research Laboratory, Center for Bio/molecular Science and Engineering; George Mason University, Klein, William; US Naval Research Laboratory, Center for Bio/molecular Science and Engineering; National Research Council Chiriboga, Matthew; US Naval Research Laboratory, Center for Bio/molecular Science and Engineering; George Mason University, Department of Bioengineering, Institute for Advanced Biomedical Research Bui, Hieu; US Naval Research Laboratory, Center for Bio/molecular Science and Engineering; National Research Council Oh, Eunkeu; US Naval Research Laboratory, Center for Bio/molecular Science and Engineering Nita, Rafaela; US Naval Research Laboratory, Center for Bio/molecular Science and Engineering; National Research Council Naciri, Jawad; US Naval Research Laboratory, Center for Bio/molecular Science and Engineering Johns, Paul; US Naval Research Laboratory, Center for Bio/Molecular Science and Engineering; American Society for Engineering Education Fontana, Jake; US Naval Research Laboratory, Center for Bio/molecular Science and Engineering Diaz, Sebastian; US Naval Research Laboratory, Center for Bio/molecular Science and Engineering Medintz, Igor; US Naval Research Laboratory, Center for Bio/molecular Science and Engineering

Nanoscale ARTICLE

Analyzing fidelity and reproducibility of DNA templated plasmonic nanostructures

Received 00th January 20xx,
Accepted 00th January 20xx

DOI: 10.1039/x0xx00000x

Divita Mathur,[†,a,d] William P. Klein,[†,a,c] Matthew Chiriboga,[a,e] Hieu Bui,[a,c] Eunkeu Oh,[b,f] Rafaela Nita,[a,c] Jawad Naciri,[a] Paul Johns,[a,g] Jake Fontana,[a] Sebastián A. Díaz,[a] and Igor L. Medintz[a*]

Synthetic DNA templated nanostructures offer an excellent platform for the precise spatial and orienational positioning of organic and inorganic nanomaterials. Previous reports have shown its applicability in the organization of plasmonic nanoparticles in a number of geometries for the purpose of realizing tunable nanoscale optical devices. However, translation of nanoparticle-DNA constructs to application requires additional efforts to increase scalability, reproducibility, and formation yields. Understanding all these factors is, in turn, predicated on in-depth analysis of each structure and comparing how formation changes with complexity. Towards the latter goal, we assemble seven unique plasmonic nanostructure symmetries of increasing complexity based on assembly of gold nanorods and nanoparticles on two different DNA origami templates, a DNA triangle and rhombus, and characterize them using gel electrophoresis, atomic force- and transmission electron microscopy, as well as optical spectroscopy. In particular, we focus on how much control can be elicited over yield, reproducibility, shape, size, inter-particle angles, gaps, and plasmon shifts as compared to expectations from computer simulations as structural complexity increases. We discuss how these results can contribute to establishing process principles for creating DNA templated plasmonic nanostructures.

Introduction

Self-assembled nanomaterials are the subject of many ongoing investigations due to their potential uses in constructing nanoscale sensing and optical devices. The burgeoning field of nanotechnology is now beginning to seek the development of useful devices as it matures and transitions from purely discovery to translational science. For electronic and optical devices, such technologies are primarily dependent upon exploiting the unique properties and characteristics of a plethora of new nanomaterials.[1, 2] Prime amongst these is a class of nanomaterials that is derived from noble metals such as gold nanoparticles (AuNPs) and gold nanorods (AuNRs).[3, 4] In such devices, AuNP and AuNR size, shape, and their arrangements or periodicities largely dictate the subsequent optical properties of the devices. The unique optical properties of these materials are principally the result of their surface plasmon resonance (SPR), which is the collective oscillation of the conduction electrons in the metallic nanomaterials that occurs when they are excited with light.[5] The plasmonic behaviour of NPs arranged in predetermined geometries can interact and manifest a localized enhancement of the electromagnetic field which is referred to as localized SPR. This is a well-known phenomenon and has been harnessed in several applications for sub-diffraction optics,[6] biosensing,[7, 8] and miniaturized electronics.[9] Critical to realizing these applications is developing new, high fidelity, and scalable methods that allow nanometer positional control of the nanomaterials especially in relation to each other.[10]

There are currently two available techniques for the bottom-up fabrication of gold-based nanodevices, which have the advantage over top-down techniques of greater scalability.[11] The first technique exploits chemical-based surface-ligand directed self-assembly.[12-14] Factors such as incubation time, relevant ligand density on the NP surface, and concentration can provide a certain degree of control over the final product. This control, however, is generally limited to one- and two-dimensional nanostructures. Templated self-assembly, the second technique, offers a versatile tool to assemble three-dimensional nanostructures.[15-17]

DNA self-assembly in particular has shown great promise for the directed self-assembly of a host of structures in the 10- to 1000 nm range. DNA structures can be constructed using the principles of DNA origami, wherein a pool of single-stranded DNA (ssDNA) molecules (called staple strands) with predetermined complementarity to a long ssDNA template (called scaffold) are allowed to hybridize under controlled thermal annealing conditions.[18] DNA-based constructs can play the role of well-defined platforms for positioning other organic and inorganic particles with < 2 nm precision due to the addressable nature of each ssDNA component and nucleotide in the DNA structures as well as the growing repository of chemistries that enable conjugation of DNA with other particles, nanomaterials, biologicals, organics, fluorophores, etc.[19]

DNA-based platforms and templates have been harnessed for the controlled placement of AuNPs and, more relevant to this report, AuNRs.[20-25] AuNRs are of particular interest because of their anisotropic optical properties. AuNRs exhibit two distinct plasmon modes, one each for their transverse and longitudinal dimensions. These are typically referred to as the

[a.] Center for Bio/Molecular Science and Engineering Code 6900, and
[b.] Optical Sciences Division Code 5600, U.S. Naval Research Laboratory, 4555 Overlook AV SW, Washington, DC 20375, USA.
[c.] National Research Council, 500 5th St NW, Washington, DC 20001, USA.
[d.] College of Science and
[e.] Department of Bioengineering, Institute for Advanced Biomedical Research, George Mason University, Fairfax, VA 22030, USA.
[f.] KeyW Corporation, Hanover, MD 21076, USA.
[g.] American Society for Engineering Education, 1818 N Street NW, Suite 600, Washington, DC 20036, USA.
† Authors contributed equally.
* igor.medintz@nrl.navy.mil
Electronic Supplementary Information (ESI) available: DNA sequences, DNA triangle schematic, AuNR/AuNP synthesis, additional AFM, TEM, AGE, COMSOL data. See DOI: 10.1039/x0xx00000x

transverse and longitudinal surface plasmon resonance (TSPR and LSPR), respectively. A series of fascinating reports have demonstrated the arrangement of short AuNRs in linear, angular, and side-by-side formats on various two-dimensional DNA nanostructures, many of which showed plasmonic enhancement in the synthesized constructs.[1, 26-32] There are also laudable examples of dynamic AuNR-DNA nanostructure constructs that demonstrate programmable reconfiguration and tuneable properties of chirality.[33-43] Gold particles positioned on DNA platforms have been applied as nucleation sites for depositing other metals such as silver which exemplifies the level of precision offered by DNA nanostructures.[44] A tutorial describing the process of synthesizing DNA platform-gold constructs is even available.[25]

Preliminary characterization of AuNR-DNA nanostructure constructs has largely been performed using agarose gel electrophoresis (AGE) with atomic force microscopy (AFM) and transmission electron microscopy (TEM), all serving to provide a coarse view of the formation efficiency of the product. It is difficult, however, to precisely gauge the quality of an entire sample (which may contain over 10^{15} particles) due to the limitations of microscopy that only makes it practical to characterize fewer than 10^{3} particles from representative experiments. Estimates of the physical properties such as inter-NP gaps and positional angles across the entire ensemble of replicate samples and whether the NPs are within the plasmonic coupling regime require higher-count characterization. One metric for determining the correct functionality of a multi-NP plasmonic complex is measuring their absorbance spectra to probe a relative shift in the LSPR peak arising from the absorbance profiles of the individual AuNRs in response to the plasmonic interaction between closely placed neighbouring AuNRs.[29, 45-47] By placing AuNRs[1] or different kinds of gold particles[32] in close proximity to each other on DNA origami substrates both bathochromic (red) and hypsochromic (blue) shifts can be effected. Absorbance spectra of AuNR complexes are highly sensitive to the dispersity of the sample (including dispersity in the AuNR starting material) and therefore, despite efforts to achieve high-level purification, they often show broad absorbance peaks and narrow plasmonic shifts which highlight the polydispersity in the AuNR arrangement on substrates such as DNA nanostructures. An entire suite of characterization strategies must become the baseline as DNA-templated plasmonics translates from proof-of-concept to more formalized application.

In order to transition to future applications, facile production methods, better characterization and purification, as well as higher precision control over AuNR/AuNP placement on these types of scaffolds must be developed. All of these are, in turn, dependent on in-depth and sometimes comparative analysis of the structures formed and this is what we address here. We evaluated seven different AuNR and AuNP arrangements on DNA origami templates for their structural fidelity, reproducibility, formation yields, and SPR properties as compared to simulation. **Figure 1** summarizes the nanostructures that were evaluated. We selected two DNA origami templates due to their simplicity and exceptional formation yields - the well-characterized DNA triangle and a lesser-utilized DNA rhombus, shown in **Figure 1a** and **1b**, respectively; both originally designed by Rothemund.[18] AFM images of the folded DNA origami templates are shown in **Figure 1c** and **1d**. In each of the seven structures a specific subset of staple strands was substituted with capture strands in order to achieve the desired NP arrangement on the DNA templates. As an example, **Figure 1e** shows eight extended staple strands (red) on one side of the DNA triangle that allowed the attachment of two 20 X 50 nm AuNRs. The surface of the AuNRs were modified with thiol-labelled ssDNA strands such that the AuNRs could attach to the DNA templates *via* complementary DNA hybridization. We evaluated arrangements of end-to-end (ETE) 20 X 50 nm AuNRs both with and without an intervening 10 nm diameter AuNP, which follows upon the work of Pal *et al.*, 2011 (**Figure 1f-i**).[29] We will refer to the configuration containing the AuNP as the rod-particle-rod (RPR) configuration. Next, we designed three new AuNR architectures by programming angular arrangement of 10 X 90 nm AuNRs on the DNA triangle and rhombus. The configurations will be referred to as the inverted-V (**Figure 1j**), the three-rod-triangle (**Figure 1k**), and the diamond, (**Figure 1l**) configuration. For each construct, we present results of AFM and TEM analysis, calculated formation yield based on AFM particle counts, and absorption profiles in relation to the corresponding individual AuNR species. We also compare predicted versus observed AuNR separation gaps and placement angles in selected structures. To further analyse the observed plasmonic behaviour, we generated COMSOL simulations of the predicted SPR properties expected from the AuNR architectures.

Overall the results show exemplary red-shift in the LSPR peaks of ETE and RPR constructs made with 20 X 50 nm AuNRs along with expected red- or blue-shifts for the 10 X 90 nm AuNR constructs thereby pointing towards the successful placement of AuNRs within the plasmonic coupling regime of each other. The 20 X 50 nm AuNR configurations align well with the COMSOL predicted LSPR shifts while the 10 X 90 nm AuNR configurations tend to vary. In the development of the entire synthesis process of these AuNR-DNA nanostructure constructs, we observed that the same DNA sequence could be utilized to capture more than one AuNR on the same DNA-based substrate. However, AuNP attachment in conjunction with AuNRs require an orthogonal capture sequence to prevent competitive binding. Secondly, the selection of capture sites on DNA nanostructures can alter the physical properties of the final AuNR-DNA nanostructure construct such as AuNR-driven DNA nanostructure dimerization. We also incorporated semi-automated size exclusion methods of purification such as fast protein liquid chromatography (FPLC) and verified that they provide usable materials in a rapid manner.

Experimental

Materials

Bacteriophage M13mp18 (abbreviated as M13; 1 μg/μL) scaffold strand was purchased from Bayou Biolabs and used without further purification. Other DNA oligonucleotides were purchased from Integrated DNA Technologies (Coralville, IA) at a final concentration of 100 μM in RNAse-free water. Dithiol-labelled DNA oligonucleotides were also purchased from IDT in lyophilized conditions and reconstituted in RNAse-free water to a concentration of 1 mM. Chemicals such as 4-(2-hydroxyethyl)-1-piperazineethanesulfonic acid (HEPES; pH 7.5), 89 mM Tris 89 mM boric acid 2 mM EDTA (TBE; pH 8.4), sodium dodecyl sulphate (SDS), NaCl, $MgCl_2$, molecular biology-grade water, tris(2-carboxyethyl)phosphine) (TCEP), and $AuCl_4$ were purchased from Sigma.

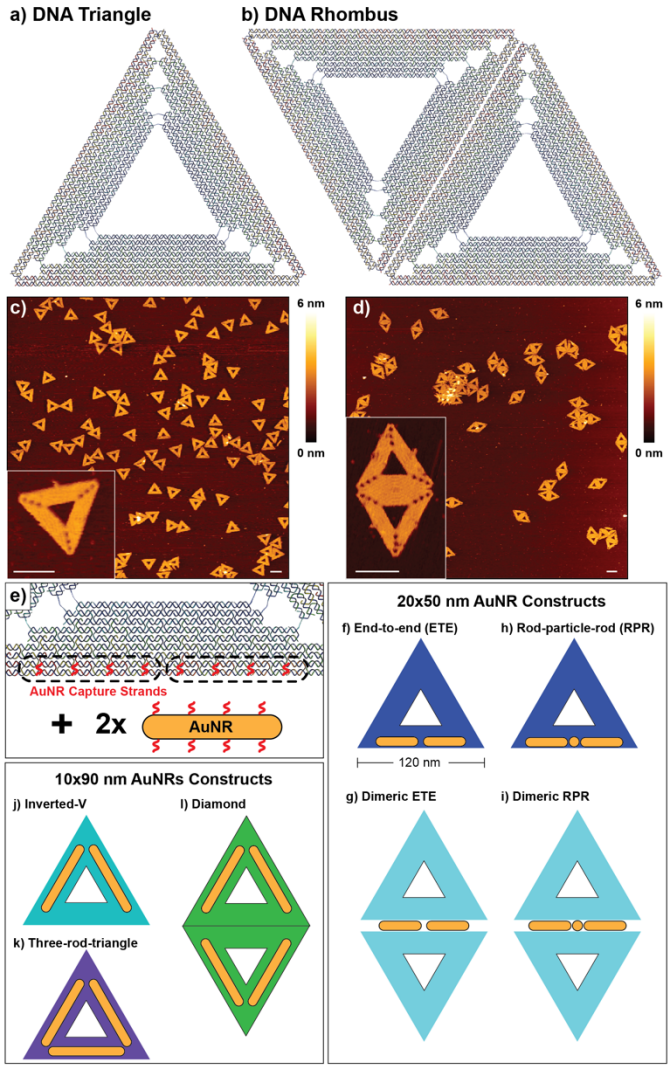

Figure 1: Schematic overview of the seven AuNR-DNA assembled arrangements that were investigated. Schematics of the DNA origami triangle (a), and the DNA origami rhombus (b). Representative AFM images of the DNA triangle (c) and the DNA rhombus (d) utilized as templates for particle attachment. Scale bars = 100 nm. (e) Representative staple capture sites. (f,h) The ETE and RPR arrangements composed of a single DNA triangle and the dimeric versions (g,i), respectively. (j-l) The three AuNR configurations, the inverted-V, the three-rod-triangle, and the diamond construct showing arrangement of 10 X 90 nm AuNRs on the DNA triangle and rhombus, respectively.

Assembly and purification of DNA origami nanostructures

Sequences for the DNA staple strands that were used to create the DNA origami triangle are listed in Supporting Information (SI) **Table S1.** Bridge staple strands that join two DNA triangles to form the DNA rhombus are specified in **Table S2.** Different staple strands in accordance with the desired AuNR/AuNP arrangement were substituted with the corresponding capture strands that are listed in **Table S4.** 5-fold excess of each staple/capture strand was mixed with M13 scaffold strand at a final total scaffold amount of 40 to 120 pmoles and concentration of 20 nM in 50 mM HEPES (pH 7.5) and 9 mM $MgCl_2$, and allowed to anneal from 85°C to 4°C at 2 minute (min) per °C. Samples were stored at 4°C until further steps. To remove excess staple strands and purify samples, the DNA structures were filtered using Amicon centrifugation filter units with a molecular weight cut off (MWCO) of 100 kDa to achieve a target volume of 200 μL of high triangle concentration (on the order of 200-500 nM). Centrifugation was performed by first rinsing the filter units with 450 μL of buffer (50 mM HEPES 9 mM $MgCl_2$) at 12,000 rcf for 1 min. Following the rinse step, 450 μL of the triangle sample was repeatedly loaded into the filter unit and centrifuged at 8,000 rcf for 5 min at 4°C until the entire sample was processed. For sample recovery, the filter unit was inverted into a fresh 2 mL recovery tube and centrifuged for 3 min at 1,000 rcf. Filter-concentrated samples were then passed through a FPLC column (Superose 6 10/300 GL column, GE ™) at a flow rate of 500 μL/min, running buffer (50 mM HEPES 5 mM $MgCl_2$ 250 mM NaCl) at 4°C by placing the column under constant refrigeration. Lastly, the FPLC-purified triangle and rhombus were buffer exchanged to eliminate NaCl from solution by passing 2-3 times through a fresh Amicon centrifugation filter (50 kDa MWCO). DNA nanostructure concentration was estimated using the Beer-Lambert Law. A_{260} was measured using a NanoDrop (Thermo Scientific) and an extinction coefficient of $1X10^8$ M^{-1} cm^{-1} was employed.[29]

AuNP and AuNR synthesis and DNA functionalization

The AuNP and AuNRs were synthesised *via* procedures that are based on previous reports and is summarized in the SI.[47-49] The DNA-functionalized NPs were prepared by incubating CTAB-stabilized AuNRs or AuNP with thiol-DNA at specific ratios determined from previously-developed methods[29, 50] and by optimizing existing procedures.[34, 51, 52] The thiol-labelled DNA used in this work are listed in the **Table S3**. The ratio of thiol-DNA to corresponding NP were as follows – 3000 thiol-DNA per 20 X 50 nm AuNR, 3500 per 10 X 90 nm AuNR, and 550 per 10 nm AuNPs. First, dithiol-DNA was incubated with the reducing agent TCEP for 30 min at room temperature to produce the reduced thiol-DNA. 10 mM of TCEP was added for every 100 μM protected dithiol-DNA in 1X TBE buffer (pH 8.4). Thiol-DNA was then purified by using disposable PD-10 desalting columns (GE Healthcare) and 1X TBE buffer as the running buffer, and collecting all the fractions containing an A_{260} readout, indicating the presence of DNA.

A solution of the as-synthesized CTAB-stabilized AuNRs was prepared in 1X TBE 0.03% SDS, to a final AuNR concentration of

3 nM (final volume was typically 100-200 mL). Using 5 N HCl, the pH of the AuNR solution was brought to pH 5.0. Purified thiol-DNA was added to the AuNR solution and the whole mixture was incubated at room temperature with constant stirring for 24 - 48 hours (h). During this incubation, NaCl (5 M) was added gradually (usually in four increments) to the solution to bring NaCl to a final concentration of 500 mM. To eliminate the unbound thiol-DNA, the pH of the solution was increased back to pH 8.0 using 10X TBE, followed by centrifugation for 30 min. The centrifugation speed was fixed based on the NP size - 10,000 rcf for 10 nm AuNP and 20 X 50 nm AuNRs, and 8,000 rcf for 10 X 90 nm AuNRs. After centrifugation, the supernatant was discarded and the pellet was resuspended in 100-200 μL 0.5X TBE 0.03% SDS and further purified using AGE. The solution was mixed with 40% glycerol and loaded into a 0.8% agarose gel in 1X TBE and subjected to 80 V/cm electric field for 2-2.5 h at 4°C. The band representing the DNA-functionalized AuNRs/AuNP was excised and extracted from the gel using Parafilm-coated glass slides. The AuNRs were concentrated by centrifugation at 8,000 rcf for 30 min with the removal of supernatant. In the case of AuNPs, Amicon centrifugation columns (100 kDa MWCO) were used to concentrate the DNA-functionalized AuNPs. Concentration of the functionalized AuNRs was determined using UV absorbance and the LSPR extinction coefficients of the corresponding CTAB-coated AuNRs. DNA should have a minimal effect on the LSPR extinction coefficient of these NPs. The extinction coefficients were referenced from Nanopartz Inc. (www.nanopartz.com) using relative size distributions; 5.14 X 10^8 and 2.0 X 10^9 M^{-1} cm^{-1} for 20 X 50 and 10 X 90 nm AuNRs, respectively. For the 10 nm AuNP, an extinction coefficients of 1 X 10^8 M^{-1} cm^{-1} was used.[49, 53, 54] Before mixing the functionalized AuNRs with DNA origami templates, we performed a Mg^{2+} screen test on the DNA functionalized AuNRs to determine their stability in the presence of the divalent cation.[51] Stability was tested in $MgCl_2$ in the range of 0 to 500 mM. Only DNA-functionalized AuNRs stable at a minimum of 50 mM $MgCl_2$ were further used in the experiments.

Functionalized AuNP/AuNR were added in pattern-specific concentration (**Table S5 and S6**) with the respective DNA origami nanostructures to a final nanostructure concentration of 5 nM. The constructs were annealed by 24 cycles between 45°C to 30°C at 2 min/°C. The DNA rhombus attachment was carried out differently from the single DNA triangle because it was observed that subjecting the rhombus to the above-mentioned anneal protocol lead to dehybridization of the bridge strands and breaking of the DNA rhombus into its constituent DNA triangles. To avoid dehybridization, the annealing program cycled between 35°C and 25°C at 2 min/°C.

AuNR-DNA nanostructure purification

After thermal annealing of AuNR-DNA origami nanostructure constructs, the samples were mixed with ~40% glycerol (acting as gel loading solution) and loaded into a 0.8% agarose gel in 50 mM HEPES (pH 7.5) 9 mM $MgCl_2$. Importantly, we observed that running the gel at room temperature until the samples passed from the loading wells into the gel (roughly 5-10 min) before transporting it into the cold room for the remainder of the separation resulted in more sample entering the gel and thus better yield. Subsequent transfer of the gel to cold room mitigated rapid heating of the gel which is typically observed in salt-containing agarose gels. Gels were typically run at 90 V/cm for 2-3 h to achieve reasonable band separation. Gel bands of interest were then excised from the gel and sample was recovered by subjecting the gel band to mechanical pressure between two Parafilm-coated glass slides. This procedure released the buffer (and sample) from the gel while gel particulates remained trapped between the glass slides.

Absorbance analysis

Absorption spectra measurements were performed on an Agilent 8453 diode array UV-vis spectrophotometer using a 1 cm path length cuvette. The concentration of AuNR/AuNP (initial and post-DNA functionalization), was determined by diluting the samples ~100 fold and using the LSPR extinction coefficients. The purified AuNR-DNA nanostructure constructs were analysed without further dilution. 120 - 200 μL of the sample was loaded into the cuvette and the absorbance spectra from 400 nm to 1100 nm was recorded. As a control the DNA functionalized AuNRs were also measured. Spectra were all normalized to correct for concentration differences and clearly show the presence of plasmon shifts.

COMSOL simulations

The LSPR shifts were evaluated in comparison to the COMSOL simulations based on a nominal 10 nm inter-AuNR/AuNP gap size. The dimensions of the individual AuNRs were chosen to be in close agreement with the TEM values and to give peak resonances at the same location as the experimental single AuNR samples (COMSOL sizes: ETE: 18 × 40 nm. RPR: 18 × 52.6 nm. Inverted-V: 15 × 78.1 nm. Three-rod-triangle: 15 × 85.7 nm. Diamond: 15 × 79.3 nm). For each scenario, higher order structures were comprised of copies of the respective individual AuNRs with gap sizes of 5, 10, or 15 nm between the AuNRs. Further details can be found in the SI.

Microscopy analysis

AFM imaging was performed on a fast-scan AFM by JPK Instruments (Germany) under the AC fast imaging mode (liquid). On a segment of freshly cleaved mica (0.9 cm diameter) mounted on a glass slide 15 μL of the sample (at a concentration typically < 5 nM) was deposited followed by 10 μL of 50 mM HEPES 9 mM $NiCl_2$ and allowed to adsorb for 2-5 min. The mica was then rinsed by submerging in molecular biology grade water and dried using nitrogen gas. After placing the mica on the AFM stage, 40-60 μL of 1X imaging buffer (50 mM HEPES 9 mM $MgCl_2$) was deposited onto the mica, and the scanning cantilever was lowered into the buffer to create a liquid "chamber" for imaging. AFM images shown in **Figure 5** were acquired on a Bruker multimode AFM using dry-tap mode. Sample prep on mica was identical to the process described above.

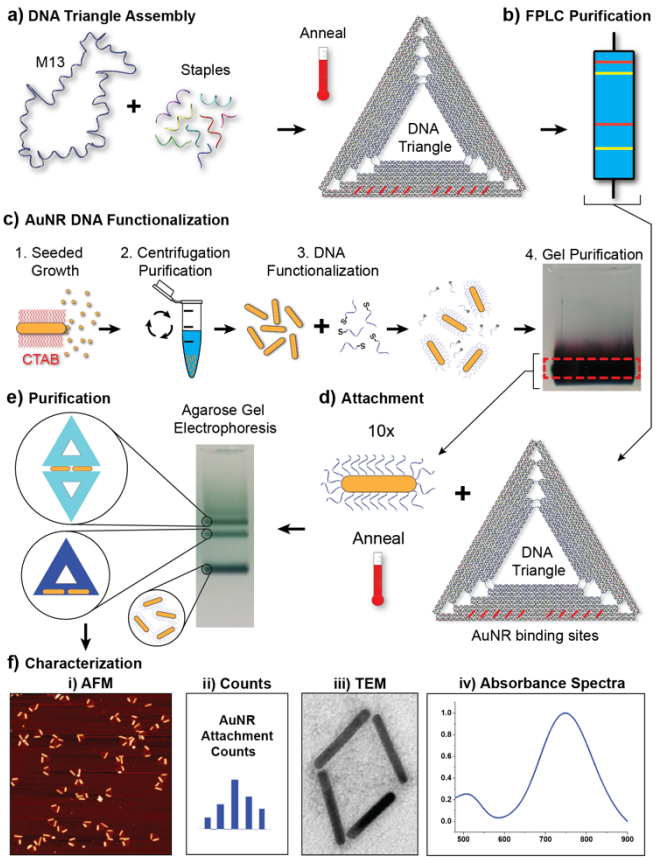

Figure 2: Schematic of the assembly, purification, and characterization of AuNR decorated DNA structures. (a) To fold the DNA triangle, M13 scaffold strand was mixed with 5-fold excess staple strands, including the capture strands. The resulting mixture was then annealed to drive the self-assembly and produce the desired DNA triangle. (b) The DNA triangle was then purified *via* FPLC. (c) The AuNRs were prepared *via* seeded growth, centrifuged as an initial purification step, then mixed with thiol-labelled ssDNA strands to yield DNA-functionalized AuNRs. Excess unbound thiol-DNA was separated from the functionalized NPs *via* AGE. Dashed red box shows the band excised to recover functionalized AuNRs from the agarose gel. (d) Purified DNA nanostructure was mixed with the functionalized AuNRs and subjected to another thermal annealing process to form AuNR-DNA nanostructure products. (e) After annealing, samples were purified using AGE to separate AuNR-DNA product from unbound functionalized AuNRs. In the case of DNA triangles as substrates, three bands were predominantly observed - functionalized AuNRs, single DNA triangle with AuNRs, and dimeric DNA triangle with AuNRs. Each band was extracted and characterized. (f) Four methods of characterization are reported for each sample - i) AFM, ii) AuNR attachment yield by particle counting of AFM images, iii) TEM, and iv) Absorption spectroscopy. These, in turn, provide information on AuNR gap analysis and placement angle.

For TEM imaging, samples were prepared on Ted Pella 01820 carbon film grids. The empty grids were pre-treated for 5 sec with the PC-2000 Plasma Cleaner (South Bay Technology, Inc.) under 75% oxygen and 25% argon conditions. Following plasma treatment, 5 to 10 μL of sample was deposited onto the grid. After 3 min excess sample liquid was removed by wicking and the residual liquid was allowed to dry in the open for 10 to 15 min. In some cases, once the sample was dry, 15 μL of Uranyl Acetate Replacement Stain 22405™ (Electron Microscopy Sciences) was deposited onto the sample grid. After 1 min the same drying technique was used to remove excess stain. Lastly, a 10 μL aliquot of water was pipetted onto the grid for rinsing and air dried. Samples were imaged on a JEOL JEM-2100 LaB6 electron microscope at 200 keV.[55] Inter-rod gap and angles were measured using ImageJ software.

Results

DNA triangle and rhombus templates

We selected the DNA triangle as the primary template for gold particle organization, as shown in **Figure 1a**. The triangle nanostructure, introduced by Rothemund, has emerged as a robust DNA architecture that has been the focus of investigation in many applications.[29, 56, 57] The wealth of available information on the DNA triangle, therefore, precludes the need for optimizing the architecture itself and here we focus on the goal of analysing AuNR placement. The DNA triangle is composed of a single molecule of M13 ssDNA scaffold that is organized into a triangular shape using 208 staple strands (**Figure S1**). The triangle self-assembly process typically results in over 90% formation efficiency *via* a simple 2 h thermal anneal process. Each side of the DNA triangle is 120 nm long with an internal cavity of roughly 60 nm that offers a wide base for the conjugation of more than one biomolecule or inorganic NP such as an AuNR. Additionally, the M13 scaffold DNA raster pattern is symmetric across all three sides of the triangle, which enables translating the symmetry into the angular placement of AuNRs on the structure.

The DNA rhombus is an extension of the DNA triangle and is new for the purpose of AuNR placement (**Figure 1b**). The rhombus architecture is derived from Rothemund's hexagon and lattice shapes by connecting two DNA triangles with bridge staple strands (**Figure S2**).[18] Interestingly, the assembly of the rhombus is also a single-pot reaction wherein the staples corresponding to individual triangle as well as the bridge staples are mixed together with the M13 scaffold strand and subjected to the same annealing program as the triangle. Intuition might lead one to think that the bridge strands would bind in solution leading to "capped" and malformed triangles, yet the multi-binding site M13 scaffold and a proper annealing strategy avoid this issue, allowing the rhombus to properly form even if there is a bridge strand or two missing. **Figure 2a** summarizes the assembly of the DNA triangle, which was performed by mixing excess staple strands with the M13 scaffold and subjecting the mixture to thermal annealing conditions. Each structure was synthesized in large quantities (> 40 pmoles), and purified using a two-step process wherein, after annealing, size-exclusion Amicon filter columns were used to concentrate the sample to < 1 mL followed by purification *via* FPLC **Figure 2b**. FPLC is a size-exclusion method of purification that has shown to have superior overall yields compared to centrifugation and gel electrophoresis.[58, 59] Amicon-based filtration of large quantities of DNA origami (> 5 mL at 20 nM) becomes time or resource intensive as it requires either increasing the number of rinse steps or the utilization of more filter units per sample. Herein, preliminary Amicon-filtration was performed once with the goal to reduce the volume of the sample, followed by FPLC

purification. **Figures S3, S4** represent FPLC results of the DNA triangle and rhombus, respectively.

AuNR/AuNP synthesis, DNA functionalization, and assembly of the AuNR-DNA nanostructures

Two different kinds of AuNRs were utilized for attachment to DNA origami structures, namely, 20 X 50 nm and 10 X 90 nm as well as 10 nm AuNPs (**Figure S5**). The two types of AuNRs were synthesized, functionalized with DNA, and purified in the lab. The procedure is outlined graphically in **Figure 2c**. It followed four main steps: 1) initial $HAuCl_4$-directed seeded growth following a previously published procedure that is based on utilizing stabilizing ligands such as cetyltrimethylammonium bromide (CTAB);[47, 48] 2) purification to remove excess CTAB; 3) thiolated-DNA functionalization *via* ligand-exchange; and 4) purification of DNA functionalized AuNRs to remove excess unattached thiolated DNA as well as gold nanospheric by-product (**Figure S6**).

Previous work has shown that there is a significant correlation between the DNA sequence of thiol-labelled DNA and the efficiency of AuNR functionalization.[51] In this role, not all DNA sequences are equivalent resulting in less than optimal thiol-DNA conjugation to the AuNR surface. AuNRs that lack robustness in their DNA functionalization fail a stability test in $MgCl_2$ supplemented buffer (the magnesium "screening") which is critical to DNA nanostructure stability and formation (**Figure S7**).[51] A poly-T sequence has been proven to demonstrate improved functionalization in comparison to some other sequences that have been used. Thus, for best attachment results, it is important to select compatible thiolated-DNA sequences. In the current work, we also sought to determine if the same DNA attachment sequences could be employed for multiple AuNP/AuNR attachment sites. We found that a common capture sequence could be used to attach two AuNRs in an ETE configuration at high yield. This minimizes design time as well as minimizes experimental complexity by allowing a single AuNR to be added in excess without having to consider individual binding site efficiencies. Thus, a poly-T thiol-labelled DNA sequence was used to functionalize the AuNRs and is referred to as the A-seq throughout the article (**Table S3**). In the case of AuNP functionalization, the procedure for synthesis and DNA attachment was slightly different, as summarized in the SI. As discussed later, an orthogonal thiol-labelled ssDNA was essential for the attachment of AuNP to the DNA triangle in conjunction with the AuNRs. To this end, a thiol-labelled DNA strand referred to as the Q-seq was employed for AuNP functionalization (**Table S3**).

To achieve each of the seven AuNR configurations, a subset of staple strands was substituted with capture strands for gold attachment. The capture strands were designed to contain extending ssDNA domains that were complementary to either the A-seq (for AuNR attachment) or the Q-seq (for AuNP attachment), listed in **Table S4**. In selecting capture sites on the DNA nanostructure, it was important to identify the maximum number of capture sites per AuNR/AuNP in order to gain maximum control over the precise positioning of each gold particle, minimize the inter-particle gap for achieving the optimum plasmon interaction, and prevent the attachment of excess gold particles by having too many capture sites. To balance these three requirements, two parameters were considered when selecting capture sites - the length of the AuNR to be attached (20 X 50 nm AuNR, 10 X 90 nm AuNR, or 10 nm AuNP) and the desired placement of the particles relative to each other. The helical turn of DNA within the triangle origami structure is ~10.7 base pair/turn, which helped identify the 5' ends of staples that emerged onto one face of the triangle. Each of these staple strands could potentially be extended with sequences to act as a capture site.[29] For optimum localization of each AuNR, maximum spatial coverage of the capture strands relative to the size of the particle was also desired. Therefore, taking this into account, along with the potential staple strands that have the correct orientation, 4, 10, and 2 capture sites for 20 X 50 nm AuNR, 10 X 90 nm AuNR, and 10 nm AuNP, respectively, were utilized.

Despite optimizing the number of capture sites ideal for different AuNR patterns, we observed variable efficiencies of attachment in the seven architectures shown here. The efficacy of AuNR synthesis and functionalization with DNA were also key factors to achieving accuracy in gold-DNA construct fabrication. At the synthesis stage, the dispersity of AuNR size could significantly become a major cause for inaccuracies in the downstream step of attachment to DNA-based substrates. We observed that in samples with AuNR length variability, the shorter rods tended to dominate the capture sites on the DNA origami structures thereby preventing the attachment of longer, and often desirable, length AuNRs. At the functionalization stage, CTAB-protected AuNRs can be difficult to functionalize along the cylindrical face of the rods due to tight packing of the ligand.[52] Incomplete functionalization, therefore, can potentially result in AuNRs that are well-conjugated with thiol-DNA strands on the ends but not along the body of the AuNRs. A direct consequence of partially functionalized AuNRs is manifest by AuNRs captured on DNA origami substrates that can pivot on the ends and, thus, attach at varying relative angles.

FPLC-purified DNA origami structures were then combined with the functionalized AuNP and/or AuNRs at pattern-specific ratios in order to promote high attachment yield (**Table S6**). The final mixture of gold nanomaterials and DNA nanostructure was subjected to a thermal anneal cyclic program for a total of 56 hours as described in the methods.[29] Based on the successful purification of DNA origami nanostructures by FPLC, we tested the utility of size-exclusion columns in the purification of the final AuNR-DNA nanostructure constructs. However, the samples suffered excessive dilution during the elution process without any enhanced efficiency in purification in comparison to AGE-based purification. The methodology would be beneficial for larger-scale production, as shown in the origami only purification, to eliminate unbound NPs. We note that as currently set-up both AGE and FPLC cannot optimally separate origami-NP structures with varying numbers of NPs due to the origami size being the dominant scale factor as far as size-exclusion is concerned. Therefore, all AuNR-DNA constructs

presented subsequently in the text were purified *via* gel electrophoresis to ensure an equivalent comparison. A representative gel is shown in **Figure 2e** of the 20 X 50 nm AuNR ETE pattern on the DNA triangle. Analysis of the gel band contents, in this example, *via* AFM revealed that the three main bands contained, from top to bottom, the dimeric ETE triangles, the single ETE triangles, and excess unattached single AuNRs. All the samples were characterized using three primary techniques, AFM, TEM, and absorption spectroscopy, as shown in **Figure 2f**, to analyse the correct formation of each construct. Again, we assert that all three are required as a baseline characterization. Absorbance was collected for each sample to assess the overall optical behaviour of the constructs relative to the corresponding DNA-functionalized single AuNRs to ensure that we were observing ensemble spectral properties. Additionally, the absorbance spectrum of each configuration was further compared to simulated COMSOL spectral profiles for the corresponding AuNR configurations. Computational modelling generated spectral profiles with inter-rod gaps of 5 nm, 10 nm, and 15 nm. Using representative AFM image data, particle count analyses was performed to determine the formation efficiency of the structures. Each fully-formed DNA structure observed in the AFM images was counted and binned for the presence of 0 - 4 AuNRs depending on the expected AuNR arrangement programmed for each sample. And lastly, inter-rod gap and angle was estimated from TEM scans.

20 X 50 nm AuNR ETE configuration

The ETE configuration of 20 X 50 nm AuNRs was designed and constructed on the DNA triangle (**Figure 1c, d**). As described above, four capture sites for each AuNR were selected on one side of the triangle for a total of eight capture sites. We expected that the two AuNRs would attach to the DNA triangles with an inter-rod gap of 10 nm. After the AuNR annealing process, the construct was purified *via* AGE, which showed three primary bands representing two annealed species and excess functionalized AuNRs (**Figure S8**). AFM and TEM images show that the two annealed species corresponded to ETE on a single triangle (**Figure 3a, b, S10, S17**) and ETE shared between two triangles (referred to as dimeric ETE; shown in **Figure 3c, d, S11, S18**). The single ETE formed with 37% efficiency, as estimated by observing over 600 particles *via* AFM analysis, with 43% and 20% particles containing one or zero AuNR attachments, respectively (**Figure 3f**). The observed average inter-rod gap was 10.2 ± 8.5 nm.

Characterization by AFM of the second band recovered from AGE showed the ETE AuNR arrangement linking two DNA triangles, referred to as dimeric ETE (**Figure 3c**). Unstained TEM scans do not have enough contrast to image DNA, therefore the construct looks similar to the single ETE arrangement (**Figure 3d**). However, high-magnification AFM scans reveal (**Figure 3c**, inset) that the AuNRs act as a bridge between two triangle structures and are thereby responsible for the dimeric nature of this construct which is different from the DNA rhombus architecture used later in this work. As the capture strands selected for ETE arrangement lie on the outer edge of one triangle side and the AuNRs are evenly functionalized along their entire surface area, the DNA on the functionalized AuNRs can hybridize with capture strands on two separate triangles thereby triggering triangle dimerization.[29] Works by Pal *et al.* and Liu *et al.* also alluded to the formation of higher-order constructs, consisting of multiple DNA triangles, but such structures were not further characterized.[29, 32] The dimeric ETE construct formed with superior efficiency indicated by the AFM

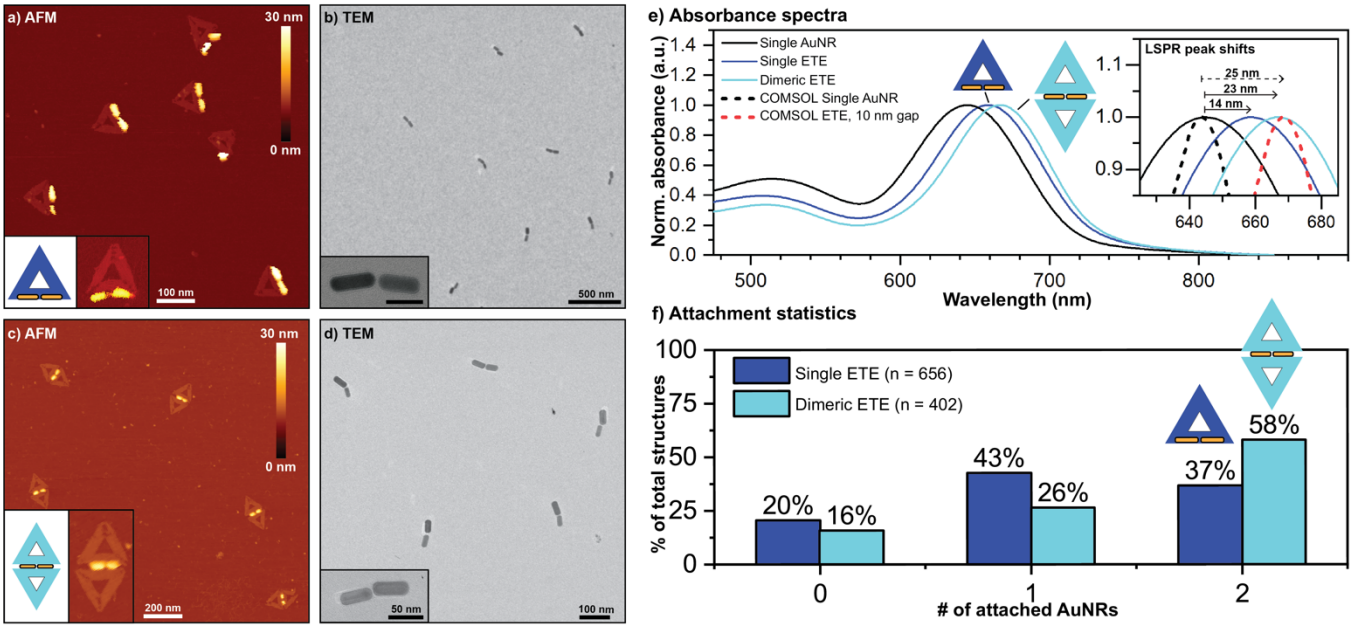

Figure 3: Characterization of ETE attachment of two 20 X 50 nm AuNRs on the DNA triangle. Two distinct products were recovered from AGE purification - AuNR attachment to a single DNA triangle (abbreviated as Single ETE) and AuNR attachment to a dimeric DNA triangle (Dimeric ETE). Shown here are representative (a), (c) AFM images, and (b), (d), TEM images of the single ETE and dimeric ETE products, respectively. (e) Absorption spectrum analysis of singe AuNR (full black line), the single and dimeric ETE configurations (dark blue and light blue lines, respectively) in comparison to COMSOL simulated LSPR peaks for single AuNR (dashed black line) and ETE configuration with a 10 nm inter-rod gap (dashed red line). Inset: Zoom in on peak position. Arrows denote peak shift: full arrows are experimental, dashed arrows are COMSOL simulations. (f) Particle count analysis based on AFM imaging of the overall formation efficiency of DNA triangle AuNR composites.

particle count analysis; nearly 60% particles showed the ETE configuration out of a total of 402 particles (**Figure 3f**). Interestingly, the inter-rod gap measured in this case was 13.7 ± 8.0 nm. This result may be initially surprising, yet the fact that a larger absorbance shift was observed though the microscopy predicted a greater rod gap distance can be accounted by two important facts. The first is that there is a larger proportion of properly formed structures in the dimeric ETE sample. The second accounts for an important distinction, the absorbance is realized with suspended particles as opposed to the surface bound structures in the microscopy. Single-layered origami in solution would be expected to have some flexibility while the optimal plasmonic shift will occur in perfectly linear systems. The dimeric structure appears to add rigidity to the overall system and therefore to the linear orientation even in solution conditions. This creates a potential second benefit to the dimeric system.

Figure 3e summarizes the absorption spectra of the two ETE products in comparison to a COMSOL-simulated profile for single AuNR and ETE arrangement with an inter-rod gap size of 10 nm. While Single ETE showed a 14 nm relative red shift, the dimeric ETE resulted in a higher shift of 23 nm, which aligned exceptionally well with the predicted red-shift of 25 nm. These values suggest that the dimerization of the triangle due to bridging AuNRs contributes to the stability of the ETE configuration, likely optimizing the orientational positioning ensuring a more linear structure, thereby enhancing the overall plasmonic activity of the construct. Moreover, the shifts observed in this case are significant in comparison to the previous observations for a similar configuration.[29] This distinctive strategy may be exploitable to increase the fidelity of linear orientation designs.

20 X 50 nm RPR configuration

The inter-rod gaps achieved in the ETE construct (10.2 ± 8.5 nm) led us to investigate whether the gap could be reduced further by placing a smaller spherical AuNP between the AuNRs to generate a RPR configuration. To this end, two additional capture sites between the eight AuNR capture sites in the ETE configuration were selected. Initially, a 10 nm wide AuNP was also functionalized with the A-seq thiol-labelled ssDNA and included with a mixture of functionalized AuNRs and DNA triangles for a single-pot synthesis of RPR constructs. However, the AuNPs competitively populated all the capture sites that were inserted for AuNR attachment thereby preventing the attachment of AuNRs (data not shown). Therefore, while it was feasible to attach two AuNRs using the same DNA capture sequences such as in the ETE configuration, it was important to functionalize AuNPs with an orthogonal thiol-labelled DNA strand (called Q-seq) that would not compete with A-seq functionalized AuNR attachment to the DNA structures. This result is of value as a general rule-of-thumb for future designs, as well as opening up basic-science questions of whether this preference is kinetically or thermodynamically driven which would need to be addressed in future investigations. Q-seq functionalized AuNPs were mixed with A-seq functionalized AuNRs and DNA triangles, and annealed in a single-pot reaction followed by purification *via* AGE. Four primary bands were recovered in which the leading two bands corresponded to

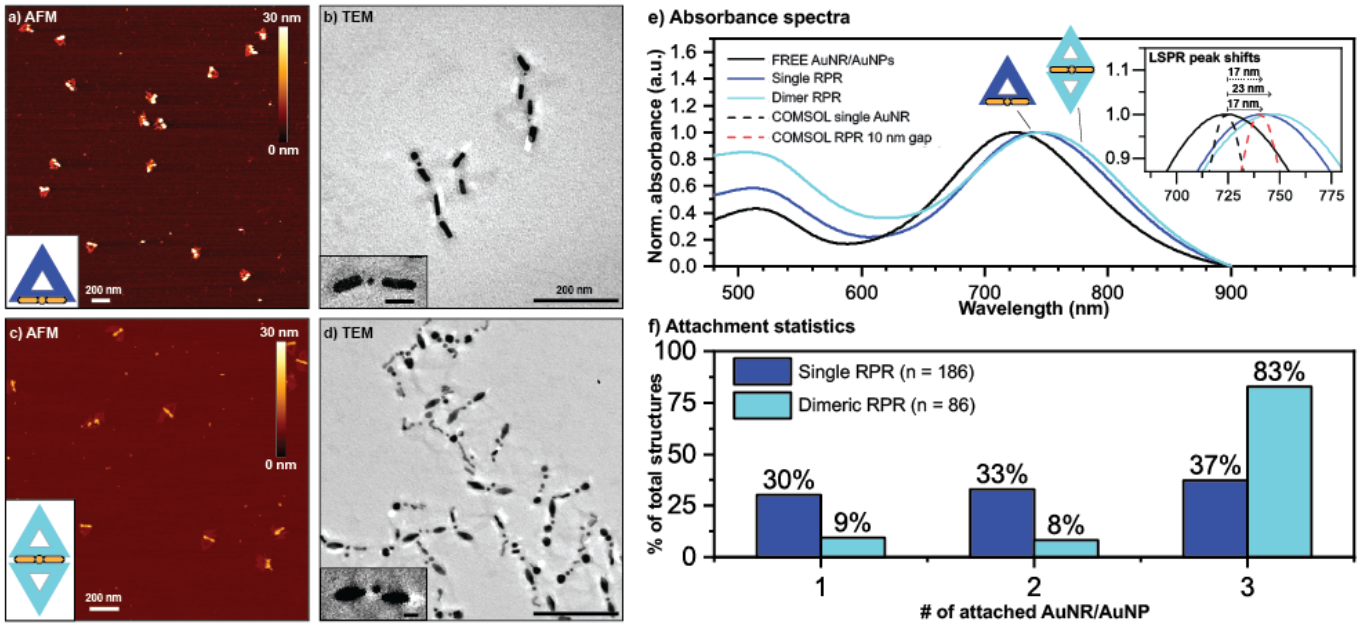

Figure 4: Characterization of the assembly of RPR arrangement of 20 X 50 nm AuNR and one 10 nm AuNP on the DNA triangle. Shown here are representative (a), (c) AFM images, and (b), (d), TEM images of the single RPR and dimeric RPR products, respectively. (e) Absorption spectra collected from the single RPR (dark blue line), the dimeric RPR (light blue line), and the single DNA functionalized AuNRs (full black line), along with COMSOL simulated spectra (dashed black and red lines). Inset: Zoom in on peak position. Arrows denote peak shift: full arrows are experimental, dashed arrows are COMSOL simulations. (f) Particle count analysis based on AFM imaging of the overall formation efficiency of DNA triangle RPR complexes.

unbound AuNRs and AuNPs (**Figure S9**). Products from the remaining two bands were recovered and analysed.

Similar to the ETE configuration, the two predominant products formed in this case were single and dimeric triangle RPR constructs. However, for unknown reasons, the DNA origami structures in the RPR constructs suffered physical deformation, as seen in the AFM images (**Figure 4a, c, S12, S13**). In the particle count analysis, we found that the single triangle RPR construct formed at ~37%, *albeit* with poorly-structured DNA triangles. On the other hand, 82% structures in the dimeric RPR construct contained the correct RPR arrangement (**Figure 4f**).

Absorption spectra of the single and dimeric RPR constructs showed red shifts of 17 and 23 nm, respectively, whereas the predicted LSPR shift for a rod-particle gap of 10 nm was estimated to be 17 nm (**Figure 4e**). The role of the 10 nm AuNP in the observed plasmon behaviour remains unclear without much further investigation on what. As before it is likely that the experimentally reported plasmonic shift is benefited by the added rigidity of the overall dimeric structure as well as the reported greater formation efficiency.

10 X 90 AuNR configurations

As mentioned previously, the SPR properties of AuNRs are highly correlated to their relative orientation as well. To this end, we sought to arrange 10 X 90 nm AuNRs in angular formats along the sides of the DNA triangle and rhombus. Three different arrangements with increasing complexity were designed: an inverted-V configuration (**Figure 1j**), consisting of two AuNRs placed at one vertex along two sides of the triangle, a three-rod-triangle configuration (**Figure 1k**) consisting of three AuNRs forming a gold-triangle on the DNA triangle, and a diamond configuration (**Figure 1l**) consisting of four AuNRs placed on the outer four sides of the DNA rhombus. For the attachment of each AuNR, 10 capture strands were integrated into the DNA origami substrates (triangle and rhombus). Unlike the linear formats of 20 X 50 nm AuNRs, the capture strands for positioning the 10 X 90 nm AuNRs were positioned one helix inward and away from the outer perimeter of the triangle edges with the goal to program an inter-rod gap of 10 nm. **Table S6** lists the various capture sites used for each configuration. Overall, the inverted-V, the three-rod-triangle, and diamond configuration had 20, 30, and 40 A-seq complementary capture strands, respectively. AuNRs bound to the inwardly positioned capture strands would be unable to bridge two triangles together to form dimeric constructs such as was observed in the ETE and RPR configurations. Therefore, by shifting the position of capture sites by a single helix on the DNA triangle, a significant degree of control can be achieved on the formation of the products. This control will be beneficial when designing linear NP structures that benefit from origami dimerization, but further still one could consider exploiting this binding methodology as an atypical tiling strategy.

Figures 5 and 6 summarize the results observed for these configurations. Due to the high number of capture sites employed in these 90 nm AuNR arrangements there was

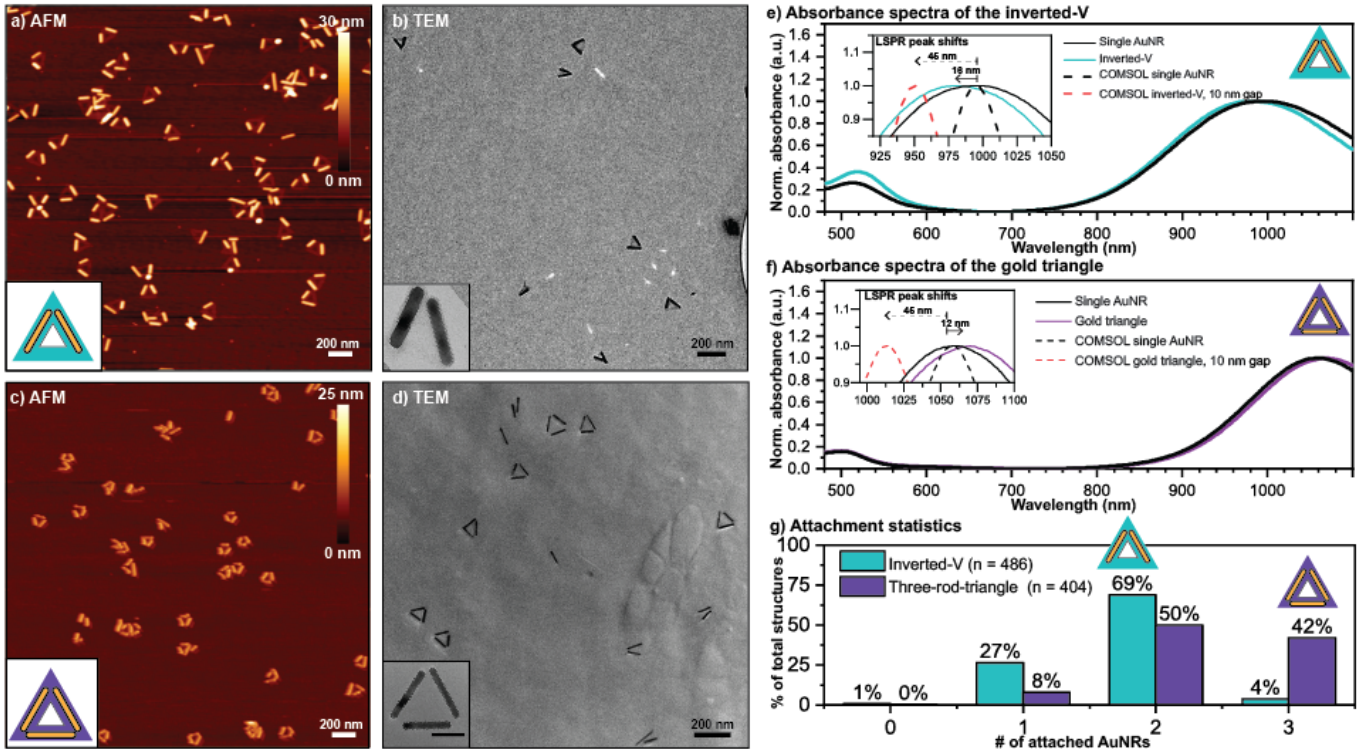

Figure 5: Characterization of inverted-V and three-rod-triangle configurations that were constructed by arranging 10 X 90 nm AuNRs on single DNA triangle templates. Representative AFM images of the inverted-V (a) and three-rod-triangle (b) configurations. TEM images of the inverted-V (b) and three-rod-triangle (d) configurations. Absorption spectra collected from the inverted-V (e) and three-rod-triangle (f) configurations. The corresponding COMSOL simulations are also included as dashed lines. Inset: Zoom in on peak position. Arrows denote peak shift: Full arrows are experimental, dashed arrows are COMSOL simulations. (g) Particle count analysis for the inverted-V and three-rod-triangle configurations.

concern for the formation of a high proportion of mis-oriented AuNRs that would overlap multiple sides of the DNA origami structures. **Figure 5a, c** (as well as **Figure S14, S15**) show representative AFM images of each construct. TEM analysis corroborated the formation of the two configurations with high fidelity (**Figure 5b, d, S21, S22**). In the case of the inverted-V, AFM analysis shows 69% formation of the correct structure whereas 27% formed only with one AuNR attached (total counted = 486; **Figure 5g**). The inter-rod angle observed was 60.9° ± 26.7° whereas the gap was 9.4 ± 7.0 nm.

Absorption characterization revealed a relative blue-shift in the LSPR peak by 16 nm in case of the inverted-V construct (**Figure 5e**). COMSOL simulation for an inter-rod gap size of 10 nm estimates a 45 nm blue-shifted LSPR peak. While the overall directionality of the plasmon shift of the inverted-V agrees with the predicted behaviour, the shift was lower than expected. We hypothesize that this is largely on account of a small sub-set of samples with angular misalignment (higher degree angle formation, as opposed to the ~60° design) which favours red-shifts. See the triangle and diamond discussion for further evidence.

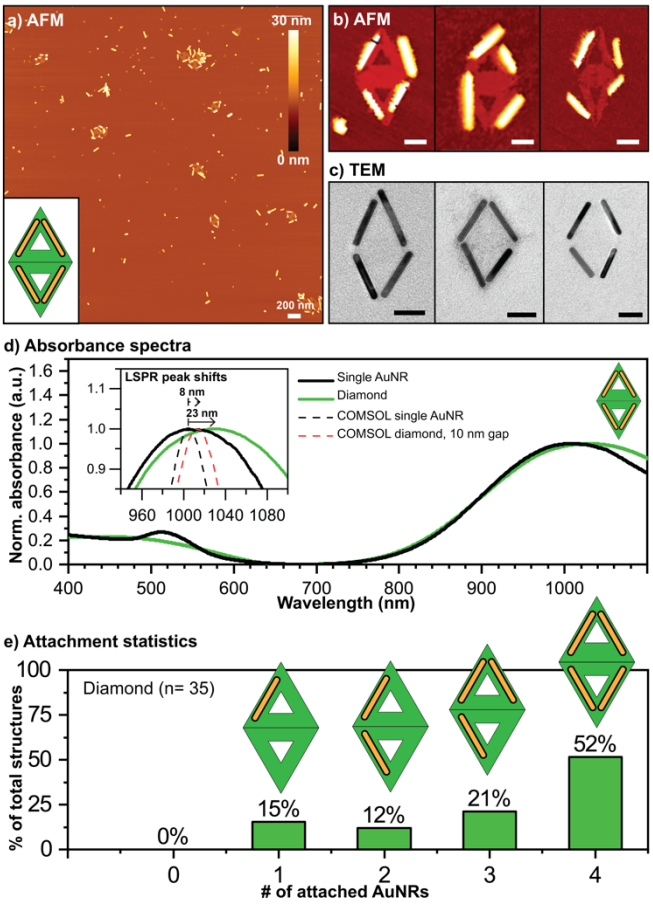

Figure 6: Characterization of the diamond configuration. (a) Representative AFM image of the diamond configuration that consisted of four 10 X 90 nm AuNRs on the outer sides of the DNA rhombus. High resolution AFM (b) and TEM (c) images of the diamond complex (Scale bar = 50 nm). (d) Absorption spectra collected from the diamond sample. Inset: Zoom in on peak position. Arrows denote peak shift: full arrow is experimental, dashed arrow is COMSOL simulation. (e) Attachment statistics for the diamond. The four possible AuNR configurations, each with a different number of attached AuNRs, are shown above the respective bar. We note that the 2 AuNR structures actually compose a mixture of 3 possible combinations (2 rods forming an obtuse angle, an acute angle, or on opposite sides of the rhombus).

AFM image of the three-rod-triangle configuration (**Figure 5c**) showed exemplary formation efficiency as corroborated by particle count analysis estimating 42% structures with three-correctly positioned AuNRs in a total of 404 counted particles (**Figure 5g**). The average inter-rod angle observed was 65.0° ± 14.8°, with a gap of 7.8 ± 5.2 nm. Absorption results showed a 12 nm red-shift in the LSPR peak (**Figure 5f**). Contrary to that, COMSOL simulations predicted a blue-shift of 45 nm. It was observed that the triangle had a greater angle value on average as compared to the inverted-V, and as such the red-shift becomes even more prevalent. The greater weight of obtuse-angled structures is demonstrated by the diamond data (*vida infra*).

Lastly, the diamond architecture was synthesized as shown in **Figure 6**. The procedure to assemble this structure was slightly different than the triangle-based structures discussed above. As the DNA rhombus is assembled using two copies of the DNA triangle joined using bridge strands, capture sites for two AuNRs were designed into two sides of the triangle which resulted in a total of four symmetric capture sites on the rhombus. The mixture of functionalized AuNRs and the DNA rhombus was carefully annealed at a lower temperature than the AuNR-DNA triangle process in order to prevent dehybridization of the bridge staple strands and consequent destabilization of the rhombus. The annealing program for attaching functionalized AuNRs on the rhombus was lowered overall by 10°C. **Figure 6a,b** (and **Figure S16**) shows a representative AFM scans of the final construct and TEM images are shown in **Figure 6c**. Particle count analysis of 35 particles indicated 52% formed with four AuNRs on the sides of the rhombus (**Figure 6e**). Only fully formed diamond structures were considered for the statistical analysis here. A closer look at the AFM images show that the sample suffered from variability in positioning of the AuNRs, resulting in poor structural fidelity. We attribute this relatively overall low formation efficiency to the inherently complex nature of the design and the quality of AuNR synthesis and functionalization as discussed previously.

A LSPR red-shift of 23 nm was observed relative to the LSPR of the single AuNRs (**Figure 6d**). COMSOL simulations predicted a 15 nm red-shift. Here it is interesting that the combination of what one could describe as two inverted-V shapes reverses the plasmon shift from hypsochromic to bathochromic. Of course, the diamond shape could also be considered as two obtuse angled-V shapes, which would result in the expected red-shift (bathochromic). The fact that the inverted-V and triangle shapes did not match the expected blue shift can potentially be accounted for by the greater than predicted angular values.

A summary of the experimental and predicted LSPR peak shifts, inter-rod gaps and angles in each configuration is provided in **Table 1**. Looking at the inter-rod measurements cumulatively, it can be seen that the positioning of the AuNRs is within the predicted value of 10 nm. However, deviation from the desired gap and angle is observed in all samples to various degrees, supporting the critical need for improved accuracy in

Configuration	# of DNA Origami Triangles	Approx. AuNR Dia. and Length	AuNP Dia.	Observed Avg. Shift Direction and Magnitude	Predicted Shift Direction and Magnitude (10 nm Gap)	Observed inter-rod gap	Predicted inter-rod gap	Observed inter-rod angle	Predicted inter-rod angle
End-to-end (ETE)	1	20 X 50 nm	N/a	Red 14 nm	Red 25 nm	10.2 ± 8.5 nm	10 nm	NA	NA
	2			Red 23 nm		13.7 ± 8.0 nm	10 nm	NA	NA
Rod-particle-rod (RPR)	1		10 nm	Red 17 nm	Red 17 nm	7.3 ± 3.4 nm	10 nm	NA	NA
	2			Red 23 nm		10.7 ± 4.7 nm	10 nm	NA	NA
Inverted V	1	10 X 90 nm	N/a	Blue 16 nm	Blue 45 nm	9.4 ± 7.0 nm	10 nm	60.9° ± 26.7°	60°
Three-rod-triangle	1			Red 12 nm	Blue 45 nm	7.8 ± 5.2 nm	10 nm	65.0° ± 14.8°	60°
Diamond	2			Red 23 nm	Red 8 nm	17.8 ± 11 nm	10 nm	72.2° ± 17.8°	60°

Table 1: Comparison of the observed and simulated LSPR shifts, inter-rod gaps and angles for the seven configurations. Simulations assume a 10 nm inter-rod gap spacing. The RPR construct represents AuNR-AuNP gap.

AuNR positioning, particularly in applications that depend on it. **Figures S23-S25** also include additional information on the COMSOL estimated properties for smaller (5 nm) and larger (15 nm) gap sized. Overall, we observed bathochromic red-shifts in the dimeric ETE, the dimeric RPR, and the diamond configurations. We also observed a hypsochromic blue-shift only in the inverted-V configuration while the prediction indicates that both the inverted-V and the three-rod-triangle configurations should be blue-shifted. Clearly, a measurement as simple as absorbance spectra can provide considerable insight into the formation fidelity of linear and angled AuNR designs.

Conclusions

DNA nanostructures have the potential to be excellent nanoscale designer platforms or breadboards for prototyping gold nanomaterial positioning and accessing their enhanced capabilities in pursuit of engineering new optical applications. In this work, we formalize an approach for developing known and new AuNR-DNA nanoconstructs that demonstrated red as well as blue-directed plasmonic shifts. Overall, the seven configurations investigated here exemplify the versatility of this methodology for creating a diverse pool of nanoscale optical devices. More importantly, the plasmonic shifts achieved by close positioning of AuNRs in the ETE configuration led to high plasmonic red shifts greater than 20 nm.

Each configuration was characterized several ways namely, AFM, TEM, absorption spectrum, particle count analysis, and COMSOL analysis, which allows a clearer understanding of the system as well as its limitations. We also include inter-rod distances and relative angles in select cases which, as metrological data, is largely absent from current work on gold-DNA origami assemblies.

In comparison, Pal et al. showed the organization of two AuNRs with relative inter-rod angles of 180°, 60°, 0°, and 90°.[29] Each AuNR was functionalized with an orthogonal thiol-labelled DNA strand and the corresponding complementary sequence was appended to selected staple strands on the DNA triangle base for DNA base-pair driven conjugation of the AuNRs. Therefore, two unique sequences were used for the attachment of two AuNRs at different positions. Characterization of different AuNR-triangle constructs was performed using AGE, TEM, and UV-vis. Formation efficiency and yield was calculated using particle count analysis on TEM scans from a total of 100 identified particles. The overall plasmon shift observed by UV-vis showed 9 nm and 6 nm red-shift in the cases of 180° and 60° relative AuNR angles, respectively, 5.5 nm blue-shift in 0° placement (parallel arrangement), and no shift for 90° relative AuNR angle. We present here similar constructs (ETE) and newer configurations (three-rod-triangle and diamond) utilizing the same capture strand for all the AuNRs which simplifies the assembly process while slightly improving formation efficiencies. More recent work by Wang and co-workers used a common capture sequence for positioning three AuNRs on a 3D DNA origami triangular frame.[32] Three kinds of patterns were designed, each containing three AuNRs arranged on the sides of the origami structure but different arrangements of spherical AuNPs. The yield observed by counting ~400 particles were in the range of 50-80% whereas both red- and blue-shifts were effected. Our approach corroborates the utility of single capture sequence for positioning more than one AuNR on a different set of architectures.

Overall, we suggest a more comprehensive approach to analysing gold-DNA fabricated constructs as this provides far-more information across the ensemble. It also allows for easier comparison between a set of related or even different structures. Of course, there are many challenges yet to be overcome in order to expand the applicability of these AuNR-DNA nanostructure constructs. Prime amongst these is just expanding the available metrological tools to clearly characterize the formation efficiency as microscopy can be destructive in nature.[60-62] Moreover, microscopic data is commonly limited to 100-200 identified particles of a sample which could often be statistically insignificant. Assembly efficiency in our configurations was generally correlated with the degree of complexity of the desired architecture; the 10 x 90 nm AuNR diamond showed the poorest formation (**Figure 6**). Clearly, when such structures are desired, they may require either extensive optimization or parallel assemblies with intensive purification to isolate and then pool the target structure. A few aspects of this optimization process were revealed here that could have a positive impact on future engineering of NP-DNA hybrids. For example, decreased annealing time can be used for some tiled systems. Leveraging FPLC or other size-exclusion procedures for initial DNA template purification was useful but could not be applied successfully to subsequent AuNR-DNA constructs as they were able to eliminate unbound AuNR but not separate imperfectly formed structures. The requirement for unique capture strands for each NP to be attached to DNA templates should be reviewed for individual design specifications as this exercise can simplify the overall procedure but should avoid capture site saturation by smaller NPs.

And lastly, unexpected higher-order complexes, such as the dimeric ETE and RPR constructs, can often possess desirable physical properties such as facilitating the precise positioning of the constituent NPs as well as adding overall solution based rigidity to the structures.

Conflicts of interest

There are no conflicts to declare.

Acknowledgements

The authors gratefully acknowledge funding from the Office of Naval Research, the U.S. Naval Research Laboratory (NRL), and the NRL-Nanosciences Institute. W.P.K., H.B., and R.N. acknowledge National Research Council Fellowships. P.J. acknowledges an American Society for Engineering Education fellowship.

Author Contributions

D.M., W.P.K., S.A.D., and I.L.M. designed experiments, analyzed data, and cowrote the manuscript; D.M. and W.P.K. performed the experiments; H.U.B. prepared DNA rhombus nanostructure; M.C., E.O., and R.N. provided electron microscopy; M.C. analyzed electron microscopy data; E.O., R.N., and J.N. provided gold nanorods and nanoparticles; P.J. and J.F. designed, simulated, and analyzed COMSOL data.

Notes and references

1. Z. Chen, X. Lan and Q. Wang, *Small*, 2013, **9**, 3567-3571.
2. S. V. Makarov, A. S. Zalogina, M. Tajik, D. A. Zuev, M. V. Rybin, A. A. Kuchmizhak, S. Juodkazis and Y. Kivshar, *Laser Photonics Rev.*, 2017, **11**, 1700108.
3. S. J. Tan, M. J. Campolongo, D. Luo and W. Cheng, *Nat. Nanotechnol.*, 2011, **6**, 268-276.
4. L. Vigderman, B. P. Khanal and E. R. Zubarev, *Adv. Mater.*, 2012, **24**, 4811-4841.
5. K. L. Kelly, E. Coronado, L. L. Zhao and G. C. Schatz, *J. Phys. Chem. B*, 2003, **107**, 668-677.
6. F. N. Gür, C. P. T. McPolin, S. Raza, M. Mayer, D. J. Roth, A. M. Steiner, M. Löffler, A. Fery, M. L. Brongersma, A. V. Zayats, T. A. F. König and T. L. Schmidt, *Nano Lett.*, 2018, **18**, 7323-7329.
7. S. A. Walper, G. Lasarte Aragones, K. E. Sapsford, C. W. Brown, 3rd, C. E. Rowland, J. C. Breger and I. L. Medintz, *ACS Sens.*, 2018, **3**, 1894-2024.
8. O. Tokel, F. Inci and U. Demirci, *Chem. Rev.*, 2014, **114**, 5728-5752.
9. E. Ozbay, *Science*, 2006, **311**, 189-193.
10. C. Noguez, *J. Phys. Chem. C*, 2007, **111**, 3606-3619.
11. J. Fontana and B. R. Ratna, *Appl. Opt.*, 2015, **54**, F61-69.
12. D. Fava, Z. Nie, M. A. Winnik and E. Kumacheva, *Adv. Mater.*, 2008, **20**, 4318-4322.
13. X. Hu, W. Cheng, T. Wang, E. Wang and S. Dong, *Nanotechnology*, 2005, **16**, 2164-2169.
14. K. G. Thomas, S. Barazzouk, B. I. Ipe, S. T. S. Joseph and P. V. Kamat, *J. Phys. Chem. B*, 2004, **108**, 13066-13068.
15. S. N. Sheikholeslami, H. Alaeian, A. L. Koh and J. A. Dionne, *Nano Lett*, 2013, **13**, 4137-4141.
16. J. Fontana, W. J. Dressick, J. Phelps, J. E. Johnson, R. W. Rendell, T. Sampson, B. R. Ratna and C. M. Soto, *Small*, 2014, **10**, 3058-3063.
17. Y. A. Diaz Fernandez, T. A. Gschneidtner, C. Wadell, L. H. Fornander, S. Lara Avila, C. Langhammer, F. Westerlund and K. Moth-Poulsen, *Nanoscale*, 2014, **6**, 14605-14616.
18. P. W. K. Rothemund, *Nature*, 2006, **440**, 297-302.
19. K. E. Sapsford, W. R. Algar, L. Berti, K. B. Gemmill, B. J. Casey, E. Oh, M. H. Stewart and I. L. Medintz, *Chem. Rev.*, 2013, **113**, 1904-2074.
20. X. Wu, C. Hao, J. Kumar, H. Kuang, N. A. Kotov, L. M. Liz-Marzán and C. Xu, *Chem. Soc. Rev.*, 2018, **47**, 4677-4696.
21. S. Julin, S. Nummelin, M. A. Kostiainen and V. Linko, *J. Nanopart. Res.*, 2018, **20**, 1-11.
22. A. Kuzyk, R. Jungmann, G. P. Acuna and N. Liu, *ACS Photonics*, 2018, **5**, 1151-1163.
23. A. Samanta and I. L. Medintz, *Nanoscale*, 2016, **8**, 9037-9095.
24. H. Bui, S. A. Díaz, J. Fontana, M. Chiriboga, R. Veneziano and I. L. Medintz, *Adv. Opt. Mater.*, 2019, **0**, 1900562.
25. Y. Au - Huang, M.-K. Au - Nguyen and A. Au - Kuzyk, *JoVE*, 2019, DOI: doi:10.3791/59280, e59280.
26. G. Dai, X. Lu, Z. Chen, C. Meng, W. Ni and Q. Wang, *ACS Appl. Mater. Interfaces*, 2014, **6**, 5388-5392.
27. J. Lee, J. H. Huh, K. Kim and S. Lee, *Adv. Funct. Mater.*, 2018, **28**, 1707309.
28. R. Nixon, W. Liu, S. Yang and R. Wang, *Bioconjugate Chem.*, 2018, **29**, 2520-2525.
29. S. Pal, Z. Deng, H. Wang, S. Zou, Y. Liu and H. Yan, *J. Am. Chem. Soc*, 2011, **133**, 17606-17609.
30. C. Shen, X. Lan, X. Lu, T. A. Meyer, W. Ni, Y. Ke and Q. Wang, *J. Am. Chem. Soc*, 2016, **138**, 1764-1767.
31. C. Zhu, M. Wang, J. Dong, C. Zhou and Q. Wang, *Langmuir*, 2018, **34**, 14963-14968.
32. W. Liu, L. Li, S. Yang, J. Gao and R. Wang, *Chemistry*, 2017, **23**, 14177-14181.
33. Z. Chen, X. Lan, Y. C. Chiu, X. Lu, W. Ni, H. Gao and Q. Wang, *ACS Photonics*, 2015, **2**, 392-397.
34. A. Kuzyk, R. Schreiber, H. Zhang, A. O. Govorov, T. Liedl and N. Liu, *Nat. Mater.*, 2014, **13**, 862-866.
35. P. K. Lo, P. Karam, F. A. Aldaye, C. K. McLaughlin, G. D. Hamblin, G. Cosa and H. F. Sleiman, *Nat. Chem.*, 2010, **2**, 319-328.
36. C. Tserkezis, L. O. Herrmann, V. K. Valev, J. J. Baumberg and J. Aizpurua, *Opt. Express*, 2014, **22**, 23851-23860.
37. P. Zhan, P. K. Dutta, P. Wang, G. Song, M. Dai, S. X. Zhao, Z. G. Wang, P. Yin, W. Zhang, B. Ding and Y. Ke, *ACS Nano*, 2017, **11**, 1172-1179.
38. Z. Zhang, S. Liu, T. Zhou, H. Zhang, F. Wang, G. Zhang, X. Wang and T. Liu, *Langmuir*, 2018, **34**, 8904-8909.
39. C. Zhou, X. Duan and N. Liu, *Nat. Commun.*, 2015, **6**, 8102.
40. T. Funck, F. Nicoli, A. Kuzyk and T. Liedl, *Angew. Chem., Int. Ed.*, 2018, **130**, 13683-13686.
41. Y. Huang, M. K. Nguyen, A. K. Natarajan, V. H. Nguyen and A. Kuzyk, *ACS Appl Mater Interfaces*, 2018, **10**, 44221-44225.
42. X. Lan, T. Liu, Z. Wang, A. O. Govorov, H. Yan and Y. Liu, *J. Am. Chem. Soc*, 2018, **140**, 11763-11770.

43. A. Kuzyk, R. Schreiber, Z. Fan, G. Pardatscher, E. M. Roller, A. Hogele, F. C. Simmel, A. O. Govorov and T. Liedl, *Nature*, 2012, **483**, 311-314.
44. M. Pilo-Pais, S. Goldberg, E. Samano, T. H. Labean and G. Finkelstein, *Nano Lett*, 2011, **11**, 3489-3492.
45. J. Fontana, N. Charipar, S. R. Flom, J. Naciri, A. Piqué and B. R. Ratna, *ACS Photonics*, 2016, **3**, 904-911.
46. D. Doyle, N. Charipar, C. Argyropoulos, S. A. Trammell, R. Nita, J. Naciri, A. Piqué, J. B. Herzog and J. Fontana, *ACS Photonics*, 2018, **5**, 1012-1018.
47. J. Fontana, R. Nita, N. Charipar, J. Naciri, K. Park, A. Dunkelberger, J. Owrutsky, A. Piqué, R. Vaia and B. Ratna, *Adv. Opt. Mater.*, 2017, **5**, 1700335.
48. H. Jia, C. Fang, X.-M. Zhu, Q. Ruan, Y.-X. J. Wang and J. Wang, *Langmuir*, 2015, **31**, 7418-7426.
49. E. Oh, D. Lee, Y. P. Kim, S. Y. Cha, D. B. Oh, H. A. Kang, J. Kim and H. S. Kim, *Angew. Chem., Int. Ed.*, 2006, **45**, 7959-7963.
50. W. P. Klein, C. N. Schmidt, B. Rapp, S. Takabayashi, W. B. Knowlton, J. Lee, B. Yurke, W. L. Hughes, E. Graugnard and W. Kuang, *Nano Lett.*, 2013, **13**, 3850-3856.
51. X. Zhang, M. R. Servos and J. Liu, *J. Am. Chem. Soc*, 2012, **134**, 7266-7269.
52. D. Shi, C. Song, Q. Jiang, Z. G. Wang and B. Ding, *Chem Commun (Camb)*, 2013, **49**, 2533-2535.
53. E. Oh, J. B. Delehanty, K. E. Sapsford, K. Susumu, R. Goswami, J. B. Blanco-Canosa, P. E. Dawson, J. Granek, M. Shoff, Q. Zhang, P. L. Goering, A. L. Huston and I. L. Medintz, *ACS Nano*, 2011, **5**, 6434-6448.
54. K. Susumu, E. Oh, J. B. Delehanty, J. B. Blanco-Canosa, B. J. Johnson, V. Jain, W. J. Hervey IV, W. R. Algar, K. Boeneman, P. E. Dawson and I. L. Medintz, *J. Am. Chem. Soc*, 2011, **133**, 9480-9496.
55. E. Oh, F. K. Fatemi, M. Currie, J. B. Delehanty, T. Pons, A. Fragola, S. Lévêque-Fort, R. Goswami, K. Susumu, A. L. Huston and I. L. Medintz, *Part. Part. Syst. Charact.*, 2013, **30**, 453-466.
56. S. Takabayashi, W. P. Klein, C. Onodera, B. Rapp, J. Flores-Estrada, E. Lindau, L. Snowball, J. T. Sam, J. E. Padilla and J. Lee, *Nanoscale*, 2014, **6**, 13928-13938.
57. S. Takabayashi, S. Kotani, J. Flores-Estrada, E. Spears, J. Padilla, L. Godwin, E. Graugnard, W. Kuang, S. Sills and W. Hughes, *Int. J. Mol. Sci.*, 2018, **19**, 2513.
58. K. F. Wagenbauer, F. A. S. Engelhardt, E. Stahl, V. K. Hechtl, P. Stommer, F. Seebacher, L. Meregalli, P. Ketterer, T. Gerling and H. Dietz, *Chembiochem*, 2017, **18**, 1873-1885.
59. A. Shaw, E. Benson and B. Hogberg, *ACS Nano*, 2015, **9**, 4968-4975.
60. C. M. Green, K. Schutt, N. Morris, R. M. Zadegan, W. L. Hughes, W. Kuang and E. Graugnard, *Nanoscale*, 2017, **9**, 10205-10211.
61. J. C. Azcárate, M. H. Fonticelli and E. Zelaya, *J. Phys. Chem. C*, 2017, **121**, 26108-26116.
62. S. Thamm, N. Slesiona, A. Dathe, A. Csaki and W. Fritzsche, *Langmuir*, 2018, **34**, 15093-15098.

Table of Contents (TOC) figure: